Supplementary Information

An atom-by-atom view of a photochemical ring opening reaction

Enliang Wang[1,2*], Surjendu Bhattacharyya[1], Keyu Chen[1], Kurtis Borne[1], Farzaneh Ziaee[1], Shashank Pathak[1], Huynh Van Sa Lam[1], Anbu Selvam Venkatachalam[1], Xiangjun Chen[2], Rebecca Boll[3], Till Jahnke[3,4], Artem Rudenko[1,†], Daniel Rolles[1,‡]

[1]*J. R. Macdonald Laboratory, Department of Physics, Kansas State University, Manhattan, KS, 66506 USA*

[2] *Hefei National Research Center for Physical Sciences at the Microscale and Department of Modern Physics, University of Science and Technology of China, Hefei 230026, China*

[3]*European XFEL, 22869 Schenefeld, Germany*

[4]*Max-Planck-Institut für Kernphysik, 69117 Heidelberg, Germany*

* elwang@ustc.edu.cn
† rudenko@phys.ksu.edu
‡ rolles@phys.ksu.edu

Contents

1. Optical setup, temporal overlap, and UV power dependent yields

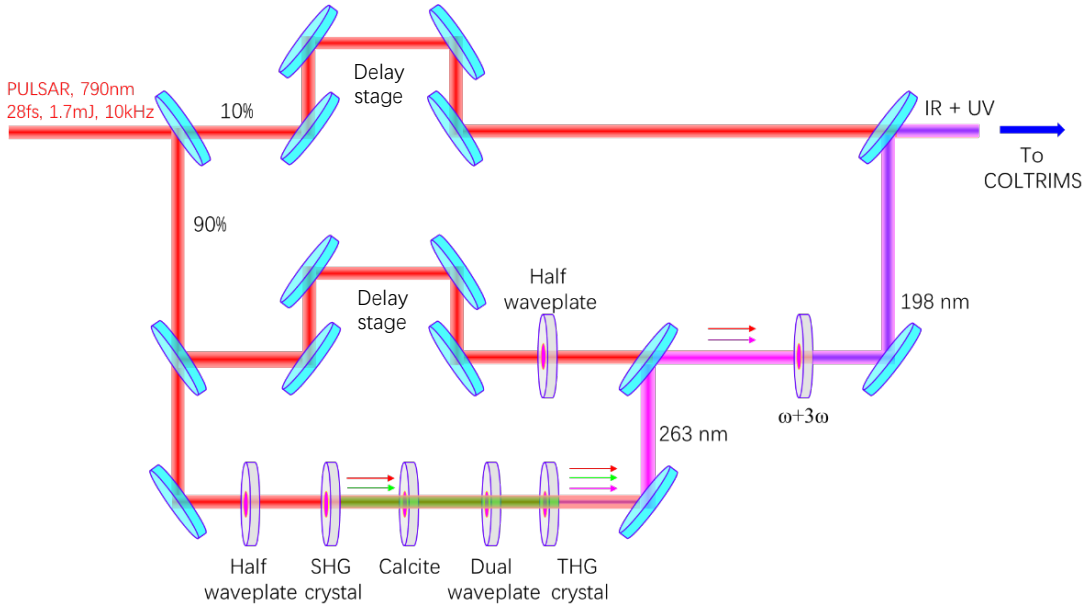

Figure S1: Sketch of the optical setup for the UV-NIR pump-probe experiment.

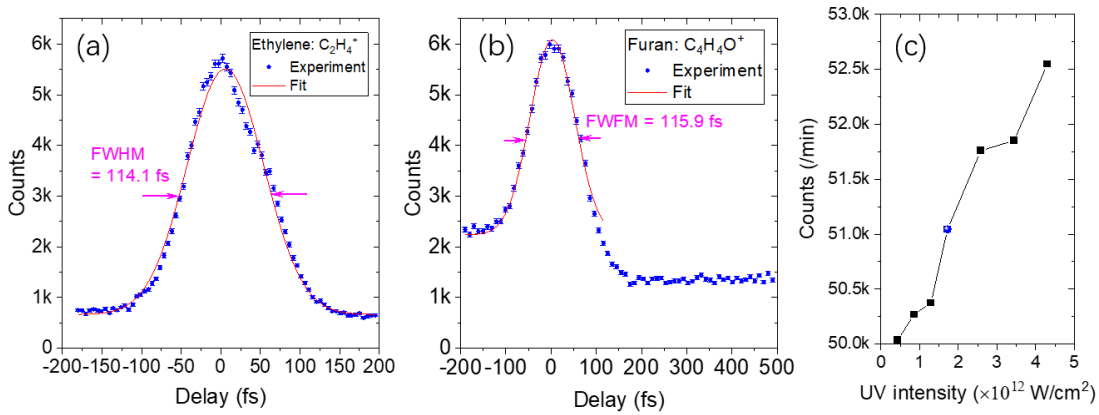

Figure S2: Delay-dependent ion yield of (a) ethylene (C_2H_4) measured with NIR and UV pulse intensities of approximately 6.7×10^{13} W/cm^2 and 1.72×10^{12} W/cm^2, respectively, and (b) furan parent cations measured under the identical laser conditions as the coincidence data shown in the manuscript (NIR: 1×10^{15} W/cm^2, UV: 1.72×10^{12} W/cm^2). The FWHM obtained by a Gaussian fit to the data is indicated. (c) Count rate of the furan parent ions as a function of UV intensity from the UV pump and NIR (1×10^{15}W/cm^2) probe experiment at an asymptotic delay of 5 ps. The solid blue point (UV intensity: 1.72×10^{12}W/cm^2; pulse energy 2 μJ) in the middle of the power scan corresponds to the intensity chosen for the pump-probe experiment shown in the manuscript. The linearity of the UV-power-dependent yield confirms that the pump-probe experiments were performed in the single-photon absorption regime.

2. Experimental kinetic energy distributions

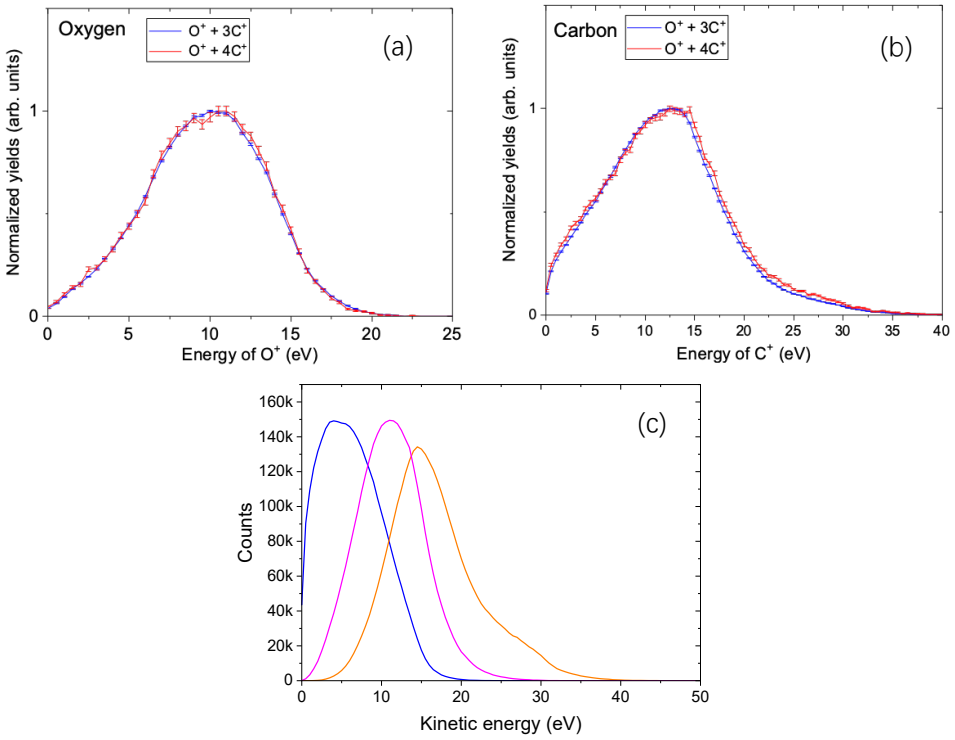

Figure S3: Experimentally observed kinetic energy distributions of (a) oxygen and (b) carbon ions for the $O^+ + 3C^+$ (blue) and $O^+ + 4C^+$ (red) coincident channels. The experimental data are normalized at their maximum. (c) Experimentally observed kinetic energy distributions of the three carbon ions of the $3C^+ + O^+$ channel sorted according to their kinetic energies: lowest (blue), medium (pink), and highest (orange).

3. Experimental normalized Newton plots for the $O^+ + 3C^+$ and $O^+ + 4C^+$ coincidence channels

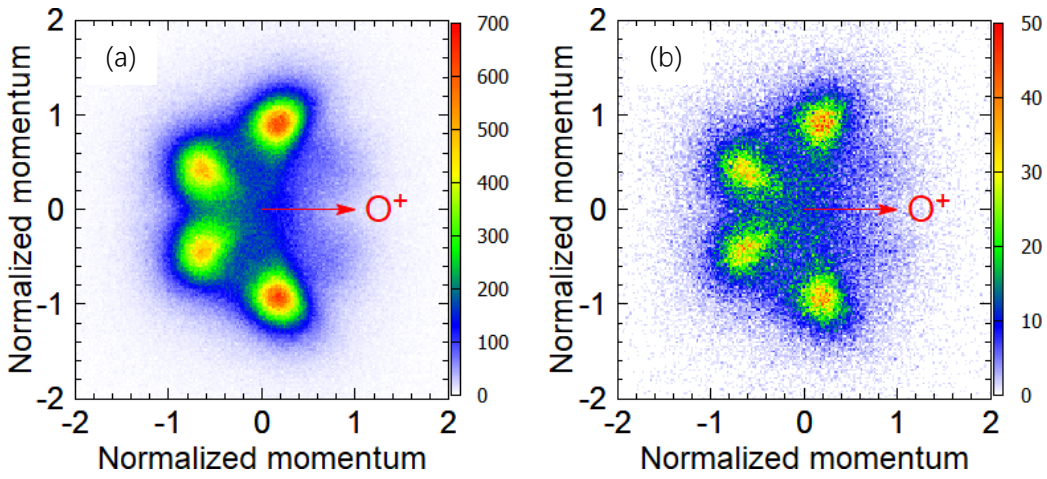

Figure S4: Experimental normalized Newton plots for the (a) $O^+ + 3C^+$ and (b) $O^+ + 4C^+$ coincident channels of the static (i.e., NIR only) measurement.

4. Geometries of furan and its isomers and transition states

Supplementary Table S1. Equilibrium geometry of furan optimized by MP2/aug-cc-pVTZ. The calculation was done using the Gaussian package (*1*).

Geometry		Coordinate (Å)		
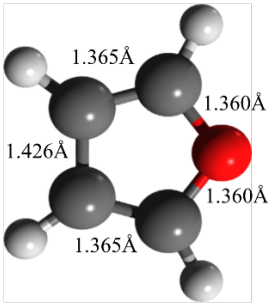	C	0.000000	1.092281	0.349397
	C	0.000000	0.712845	-0.961844
	C	0.000000	-0.712845	-0.961844
	C	0.000000	-1.092281	0.349397
	O	0.000000	0.000000	1.159765
	H	0.000000	2.044605	0.848128
	H	0.000000	1.371827	-1.812505
	H	0.000000	-1.371827	-1.812505
	H	0.000000	-2.044605	0.848128

Supplementary Table S2. Geometry of furan at the ring-opening conical intersection point. This geometry was adopted from Oesterling et al. (*2*) (optimized by CASSCF SA2/6-31G*).

Geometry		Coordinate (Å)		
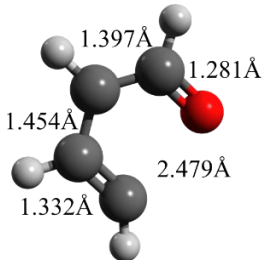	C	0.025836	-1.016724	1.205215
	C	-0.004221	0.313556	1.262174
	C	0.006874	1.110572	0.045786
	C	0.049989	0.449895	-1.184541
	O	0.079305	-0.827734	-1.266453
	H	0.027242	-1.829112	1.900533
	H	-0.037229	0.819814	2.214247
	H	-0.016948	2.182358	0.085406
	H	0.059461	1.003467	-2.111898

Supplementary Table S3. Geometry of furan at the ring-puckering conical intersection point. This geometry was adopted from Oesterling et al. (*2*) (optimized by CASSCF SA2/6-31G*).

Geometry		Coordinate (Å)		
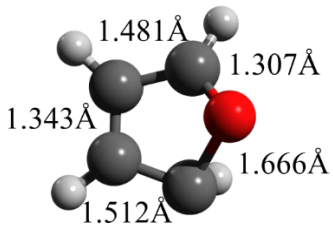	C	-0.912929	-0.032063	-0.678576
	C	-0.593812	-0.104519	0.765743
	C	1.262193	0.163146	-0.601778
	C	0.734471	0.087930	0.813520
	O	-0.103325	0.720065	-1.376042
	H	-1.717642	-0.526938	-1.193275
	H	-1.321290	-0.171420	1.552270
	H	1.356540	0.203253	1.679011
	H	1.304095	-0.837293	-1.026087

Supplementary Table S4. Equilibrium geometry of the ring-opened isomer of furan, optimized by MP2/aug-cc-pVTZ using the Gaussian package (*1*).

Geometry		Coordinate (Å)		
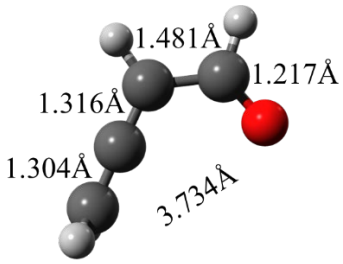	C	-2.131000	-0.409000	0.000000
	C	-1.023000	0.279000	0.000000
	C	0.116000	0.938000	0.000000
	C	1.420000	0.236000	0.000000
	O	1.560000	-0.973000	0.000000
	H	-2.599000	-0.701000	-0.931000
	H	-2.598000	-0.701000	0.931000
	H	0.120000	2.022000	0.000000
	H	2.298000	0.904000	0.000000

Supplementary Table S5. Geometry of the transition state of ground-state furan connecting the equilibrium geometry with the ring-opened isomer. This geometry was optimized by B3LYP/cc-pVT using the Gaussian package (*1*).

Geometry		Coordinate (Å)		
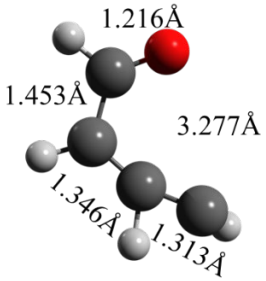	C	1.880527	-0.666703	-0.154604
	C	1.049225	0.333697	0.028533
	C	-0.115154	1.009842	0.020011
	C	-1.333443	0.217508	-0.003315
	O	-1.376759	-0.997865	0.005143
	H	2.433649	-1.121282	0.665857
	H	2.113098	0.836477	-0.043124
	H	-0.155386	2.086651	0.02946
	H	-2.264215	0.815008	-0.037091

5. Ground-state reaction coordinate

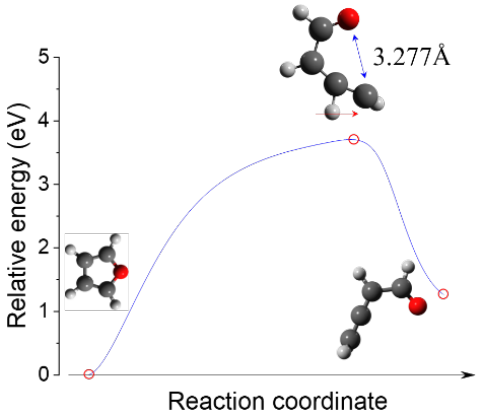

Figure S5: Reaction coordinate connecting the equilibrium geometry to the ring-opened isomer via the transition state shown in **Supplementary Table S4**. The reaction coordinate was calculated by the B3LYP/cc-pVTZ method.

6. Images of the molecular orbitals

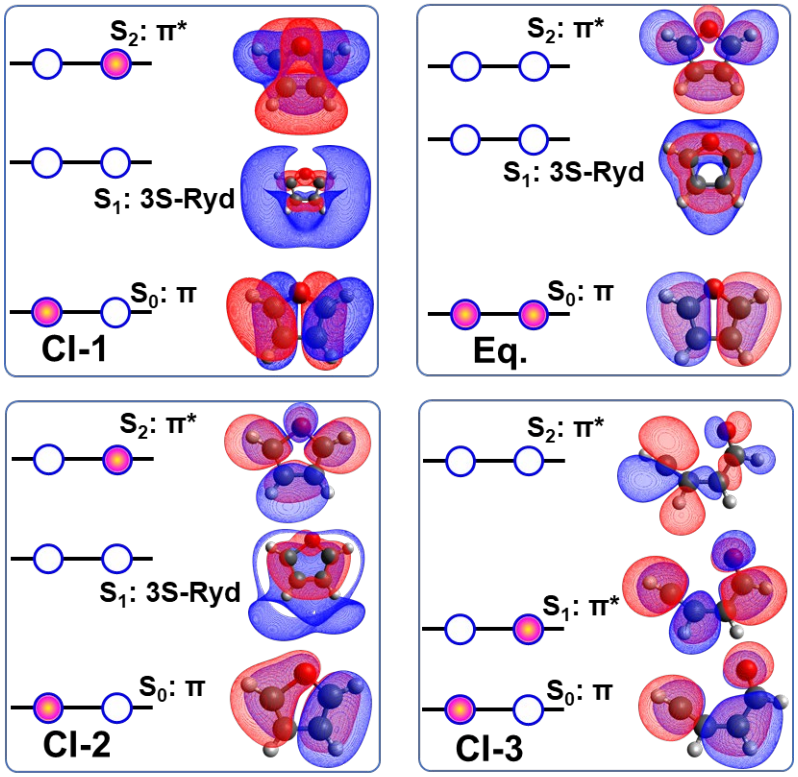

Figure S6: Orbital maps of the ground singlet S_0 and the first (S_1) and second (S_2) excited singlet states for the equilibrium geometry (Eq.) and the three conical intersection points (CI-1, CI-2, and CI-3) of furan shown in Fig. 1**b** of the main text. The orbital maps are calculated by the B3LYP density functional method with aug-cc-pvtz basis set. The calculation was performed with the PSI4 package (*3*).

7. *ab initio* molecular dynamics (AIMD) simulations and Coulomb explosion imaging simulations

The molecular dynamics on the excited states were simulated using surface hopping by combining the Newton-X (*4*) and Gaussian package (*1*). The excited-state energy gradients were calculated by the Gaussian package using time-dependent density functional theory (TDDFT) with Becke's three-parameter hybrid method using the Lee-Yang-Parr correlation (B3LYP) functional and 6-311G** basis set. The nuclear variables were driven by Newton's equations propagated in a single electronic state with a step size of 0.5 fs. In total, 55 trajectories were simulated, and 39 of them (71%) were found to end up in the ring-opening reaction path.

As the surface hopping calculations are time consuming, they were terminated once

the electronic ground state was reached. The molecular dynamics on the ground state were subsequently simulated by the Atom Centered Density Matrix Propagation molecular dynamics (ADMP) method (*5*-*7*) with the cc-pvdz basis set by the Gaussian package (*1*). The molecular geometry of the ring-opening conical intersection was chosen as the initial geometry for the simulations. To guide the simulations towards the ring-opening reaction pathway, the C-O internuclear distance was further elongated by 0.75 Å, leading to a geometry which is very close to the transition state in **Table S5**. The coordinate was distorted by randomly shifting the atomic positions within ± 0.1 Å range, and an initial internal energy of 2.5 eV was assumed. This sampling method mimics the possible geometries around the transition state and the molecular vibrational energy obtained during the electronic decay from the Franck-Condon region to the ring-opening conical intersection point. On the ground state, 116 and 98 trajectories were performed for ring-closing and ring-opening reactions, respectively. The simulation time range and time step are 500 and 0.2 fs, respectively.

The surface hopping trajectories are summarized in **Fig. S7**. Most of the S_1 to S_0 transitions happen at about 70 fs, which is in agreement with the results of the previous study by Fuji et al (*8*). Therefore, the time zero of the ground state AIMD simulations was shifted by 70 fs when comparing to the experimental results. For the trajectory displayed in **Fig. S7(d)**, some snapshots of the molecular geometries are shown, and a movie of this trajectory is included as **Supplementary Movie 1**.

An exemplary trajectory of the ring-closing and ring-opening reaction of the electronic ground state is shown in **Fig. S8 (a)** and **(b)**, respectively. The former shows large-amplitude vibrations, which are characteristic for the "hot" furan molecules formed after ring closing. For the ring-opening path, proton transfer from central carbon to terminal carbon is observed within 50 fs. The proton transfer leads to a saturated terminal carbon which is crucial for preventing renewed formation of the C-O chemical bond, i.e., for preventing the ring closing. The proton transfer is also reflected in the internuclear distance between the moving proton and the terminal carbon shown in **Fig. S9 (a)**.

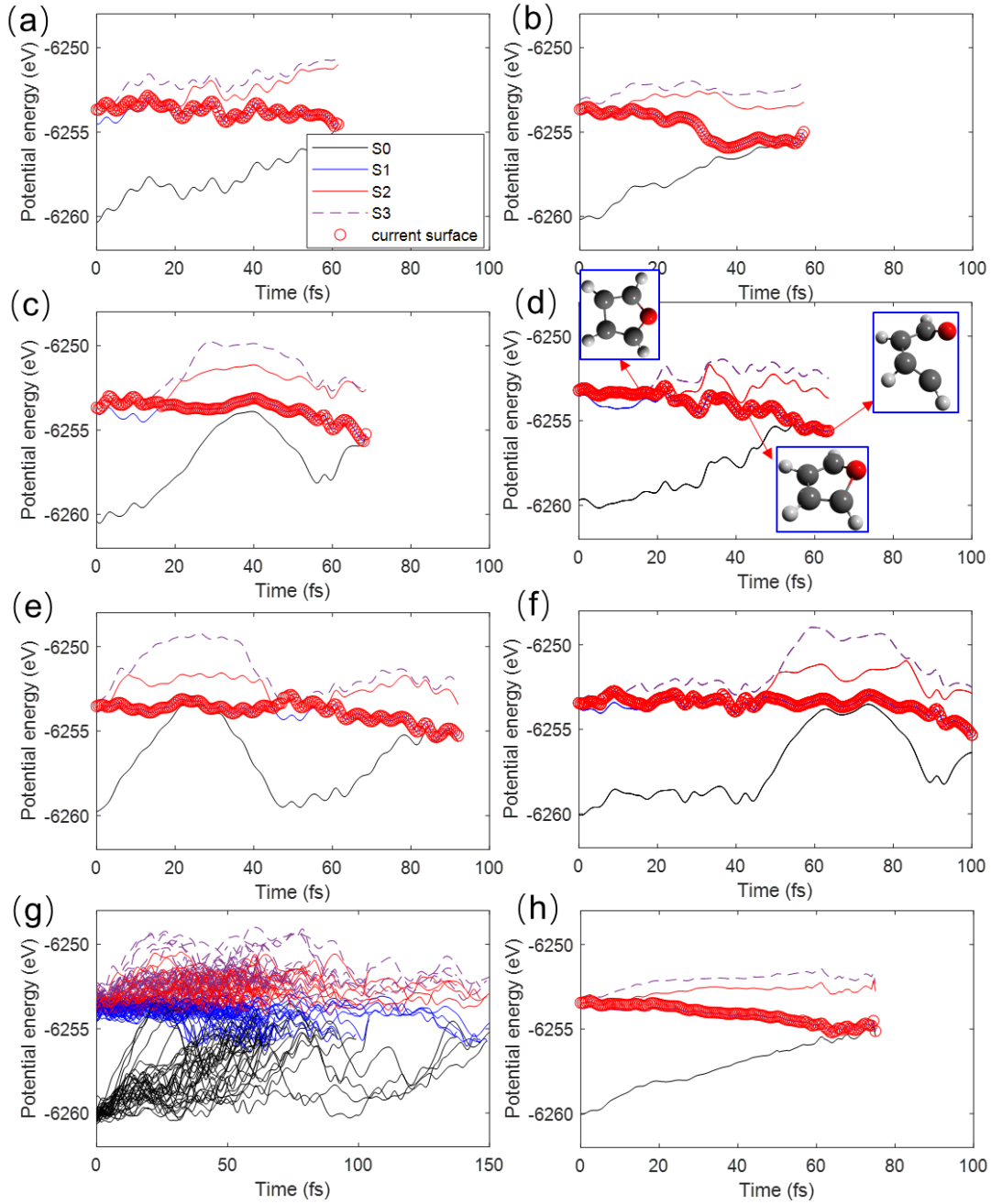

Figure S7: Surface hopping trajectories represented by the potential energy of the involved states as a function of time. Arbitrarily chosen sample trajectories show the cases where the transition from S_1 to S_0 occurs at a time shorter than 70 fs (a)-(b); close to 70 fs (c)-(d); and longer than 70 fs (e)-(f). (g) Overview of all of the trajectories of the ring-opening reactions. (h) Average of all the trajectories reaching the ring-opening conical intersection within 50-100 fs. The averaged trajectory indicates that the $S_2 \rightarrow S_1$ and $S_1 \rightarrow S_0$ transition happens at approximately 10 and 70 fs, respectively.

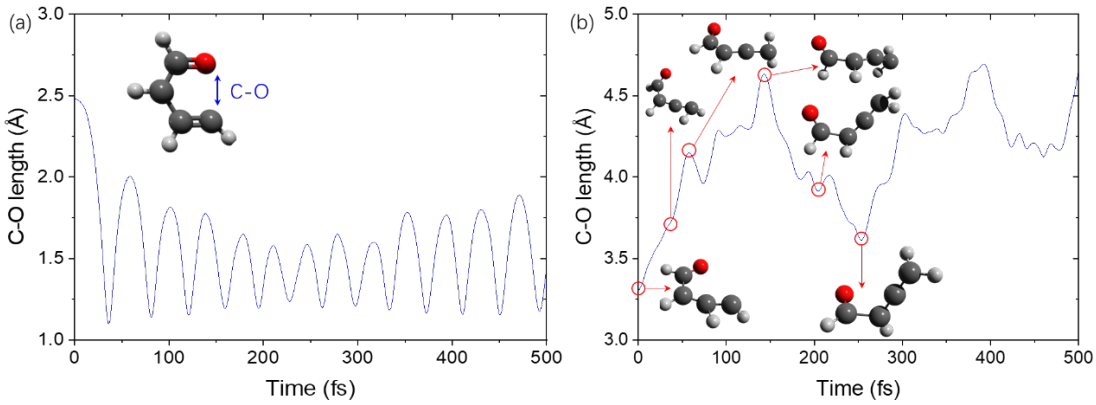

Figure S8: Trajectories of the ring-closing (a) and ring-opening (b) paths on the ground state.

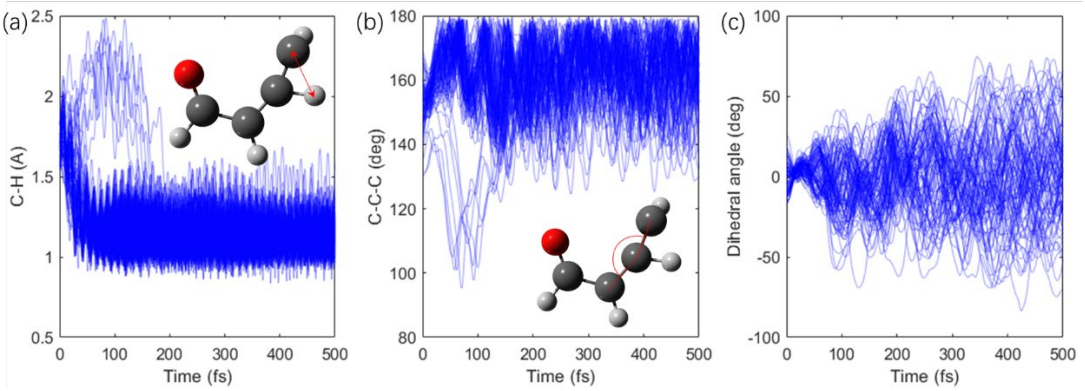

Figure S9: (a) Simulated C-H internuclear distance distributions; (b) C-C-C relative angle distributions; and (c) the dihedral angle distribution obtained from the AIMD simulations of the ring-opening path. The dihedral angle in (c) is defined as the angle between the plane of the bending O-C-C and C-C-C carbon chain.

Following the (AIMD) simulations, classical Coulomb explosion simulations (CES) were performed to model the experimental observables using the trajectories from the AIMD. The positions and velocities of every atom were extracted every 1 fs and 5 fs for the surface hopping and ground state trajectories, respectively. For the CES, we assume that every atom in the molecule carries a point charge of +1e and that all the charges are created instantaneously.

The resulting normalized Newton plot for the simulated Coulomb explosion of furan in the equilibrium geometry is shown in **Fig. 2c** of the main text and is in good agreement with the experimental results.

8. Identifying different carbons atoms of the ring-opened structure

Fig. S10 shows the simulated kinetic energies of C^+ and O^+ for the Coulomb explosion of furan in the equilibrium geometry (left panel) and a ring-opening isomer of furan (right panel). While the carbon ions resulting from the Coulomb explosion of the equilibrium geometry have similar kinetic energies, the kinetic energies of the carbon ions resulting from the ring-open isomer vary drastically depending on the site. This trend is also seen equally clearly in the CES based on the ring-opening trajectories simulated by the AIMD, shown in **Fig. S11**. The terminal carbon (C4) and the center carbon in the carbon chain (C3) have the highest and lowest average energies, respectively, whereas the kinetic energy distributions of the two carbons closest to oxygen (C1 and C2) strongly overlap. The average values of the kinetic energies of four C^+ ions as a function of time are shown by the red curves in **Fig. 11**. For quantitative comparison, the average values and their differences are summarized in **Fig. 12**.

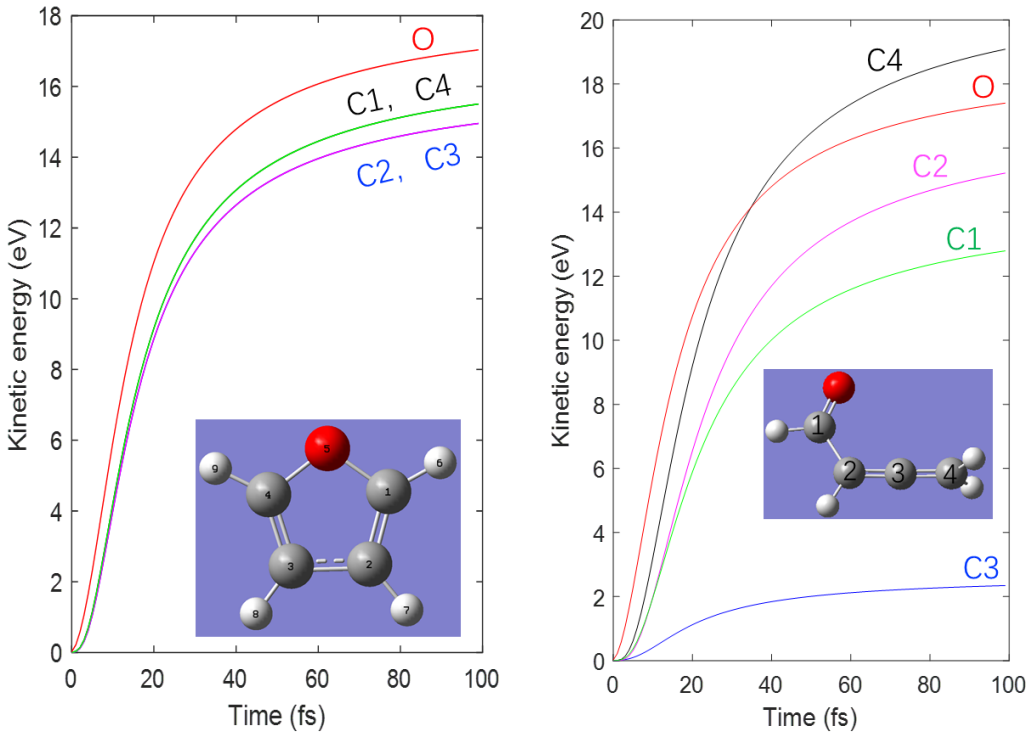

Figure S10: Simulated time-dependent kinetic energies of the ionic fragments for the Coulomb explosion of furan in the equilibrium geometry (left panel) and for the ring-open isomer of furan (right panel).

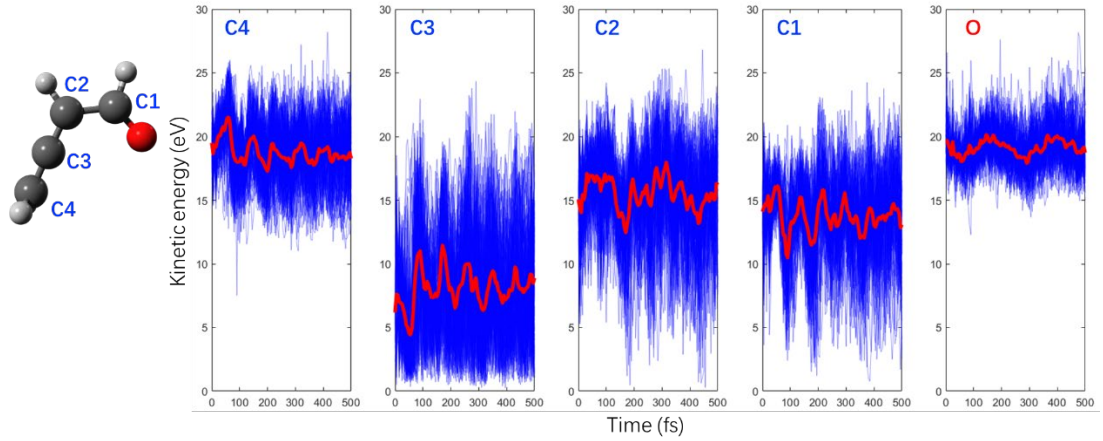

Figure S11: Kinetic energy of the carbon and oxygen ions from the CES of the AIMD trajectories as a function of time. The red curves represent the average values of the trajectories at each time. The time zero corresponds to the conical intersection of S1 → S0.

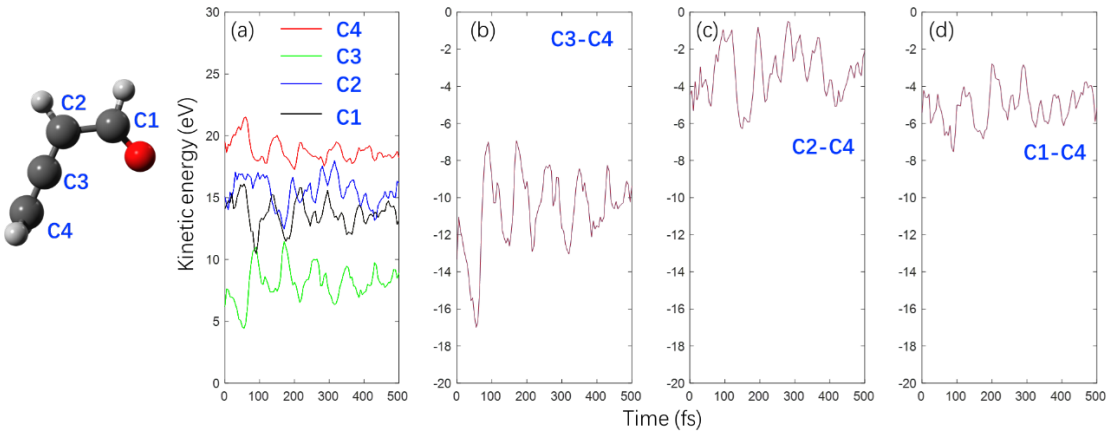

Figure S12: (a) Average kinetic energies of the four carbon ions from the CES of the AIMD trajectories. The four curves are identical to the red dots in Fig. **S11** and are summarized here once more in one panel for better comparison. (b) – (d) Kinetic energy differences between the two carbon ions indicated in the legend of each panel. The time zero corresponds to the conical intersection of S1 → S0.

To define the "molecular plane" for the Newton plots of the pump-probe data, we choose the oxygen ion and the carbon ion with the *second* highest kinetic energy. Since each analyzed coincidence event has three detected carbon ions, the carbon ion with the second highest kinetic energy corresponds, with very high likelihood, to C1 or C2. C3 and C4 are a less suitable choice for defining the plane since the ring-open isomer can be highly non-planar due to possible rotations around each of the single bonds.

9. Definition of the Newton plots

In order to build the Newton plots from the experimental or simulated fragment ion momenta, the momentum vectors were rotated in two steps, as shown in Fig. **S13**, where the solid red arrow and solid blue arrow represent the momentum vector of the oxygen and one of the carbon ions, respectively. Firstly, all momentum vectors were rotated by $-\varphi_1$ and, then, by $-\vartheta_1$ to align the oxygen momentum vector to the *x*-axis of the Newton plot. Next, the vectors were rotated by $-\varphi_2$ to rotate the selected carbon ion into the upper (+y) half plane of the Newton plot (or, alternatively, by $\pi - \varphi_2$ into the lower (-y) half plane).

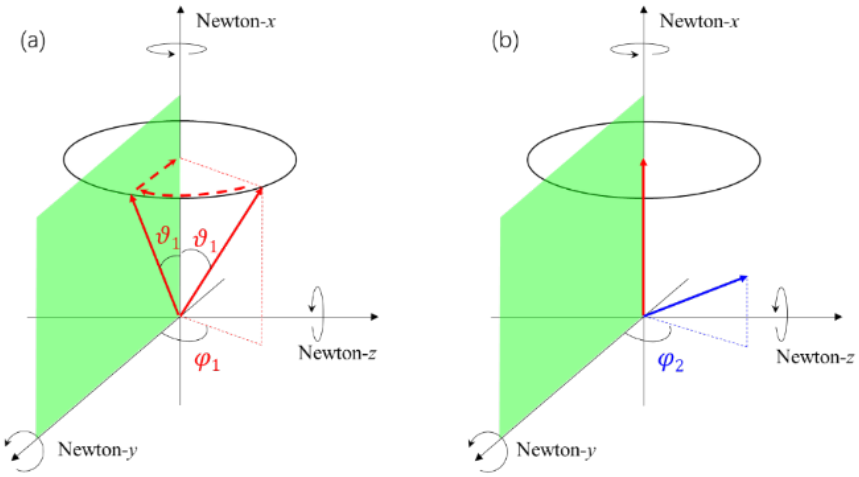

Figure S13: Schematic view of how to rotate the momentum vectors to the Newton plot plane. (a) Rotating the molecule by align the momentum vector of oxygen to the Newton-*x* axis. (b) Rotating the molecule to the Newton plot plane by the momentum vector of the selected carbon.

10. Time-resolved experimental Newton plots for the $3C^+ + O^+$ channel

In this section, we show the experimental normalized and non-normalized Newton plots on the three planes, which are the x/y, x/z, and y/z planes, as a function of the pump-probe delays from -200 to 500 fs binned in time step of 25 fs.

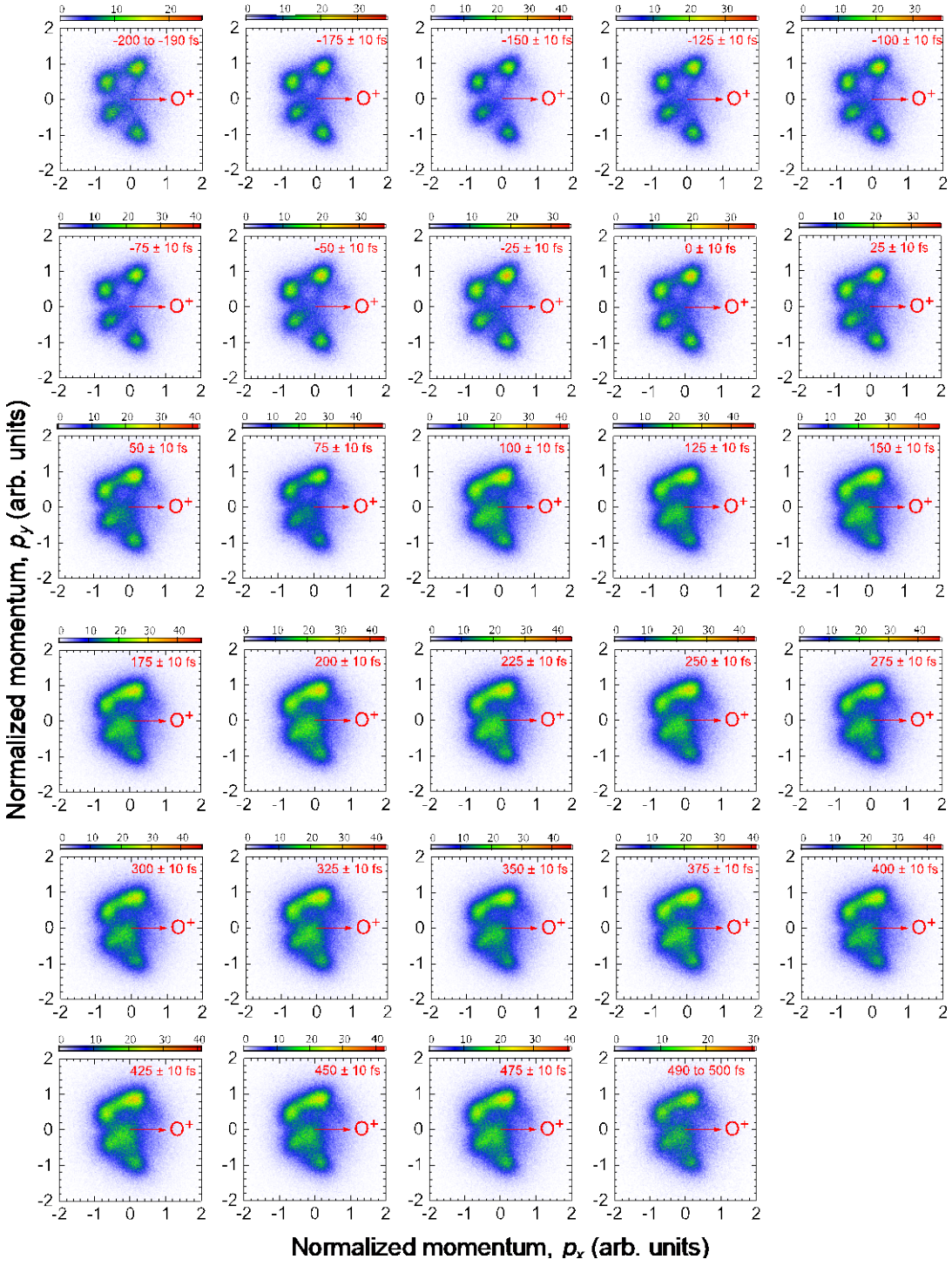

Figure S14: Experimental *normalized* Newton plots in the *px/py* plane.

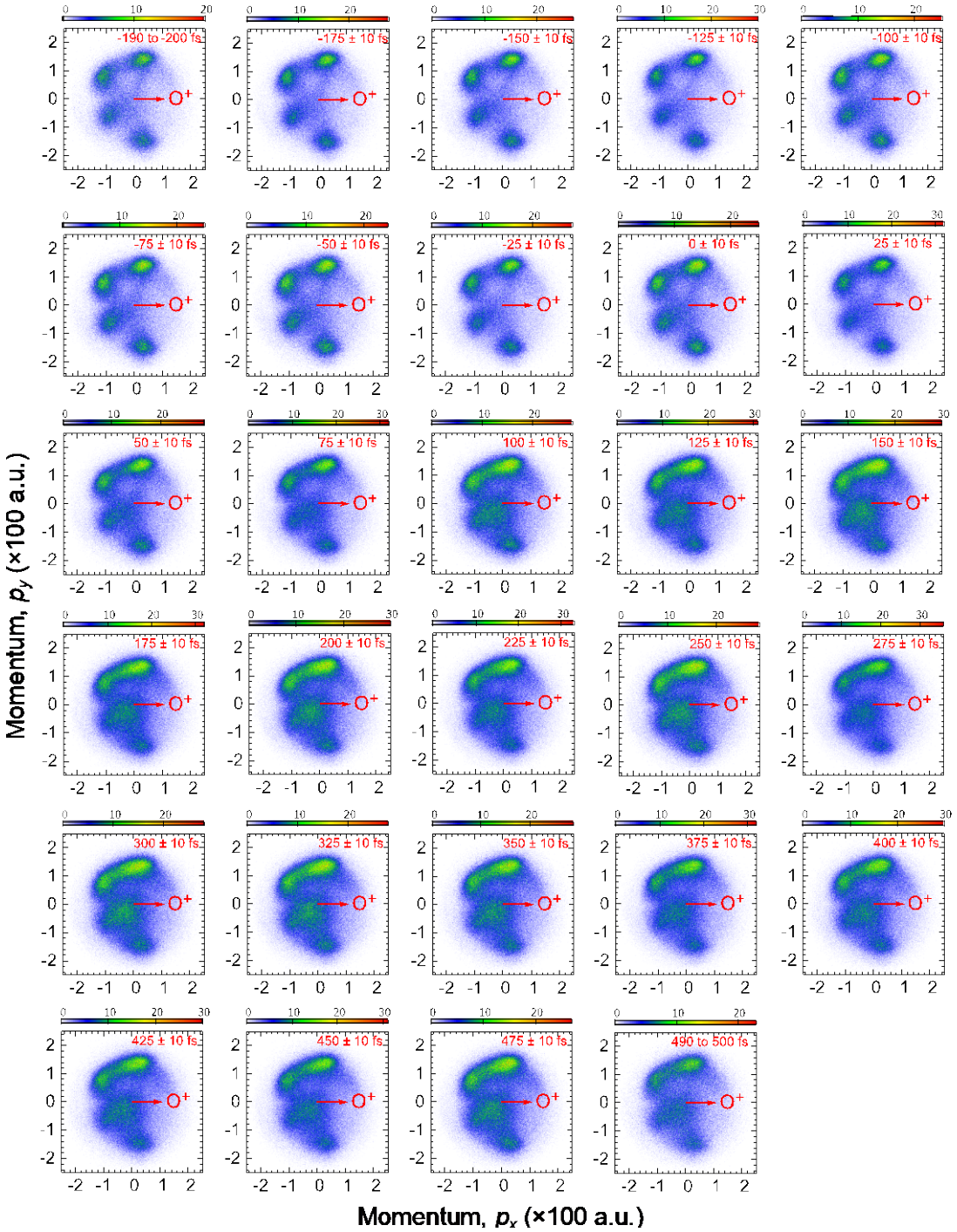

Figure S15: Experimental *non-normalized* Newton plots in the *px/py* plane. The red arrow shows the emission direction of the O^+ reference ion. The length of the arrow in this non-normalized plot was arbitrarily chosen for illustration purposes only. The mean momentum of the O^+ ion in this four-fold coincidence channel is 154.1 a.u. (with 103.9 a.u. FWHM).

For the images in the *px/pz* and *py/pz* planes, the *pz* momentum component of the carbon, which is selected to define the molecular plane, is zero. The image of this carbon is a straight line in these two planes and is not shown in these figures.

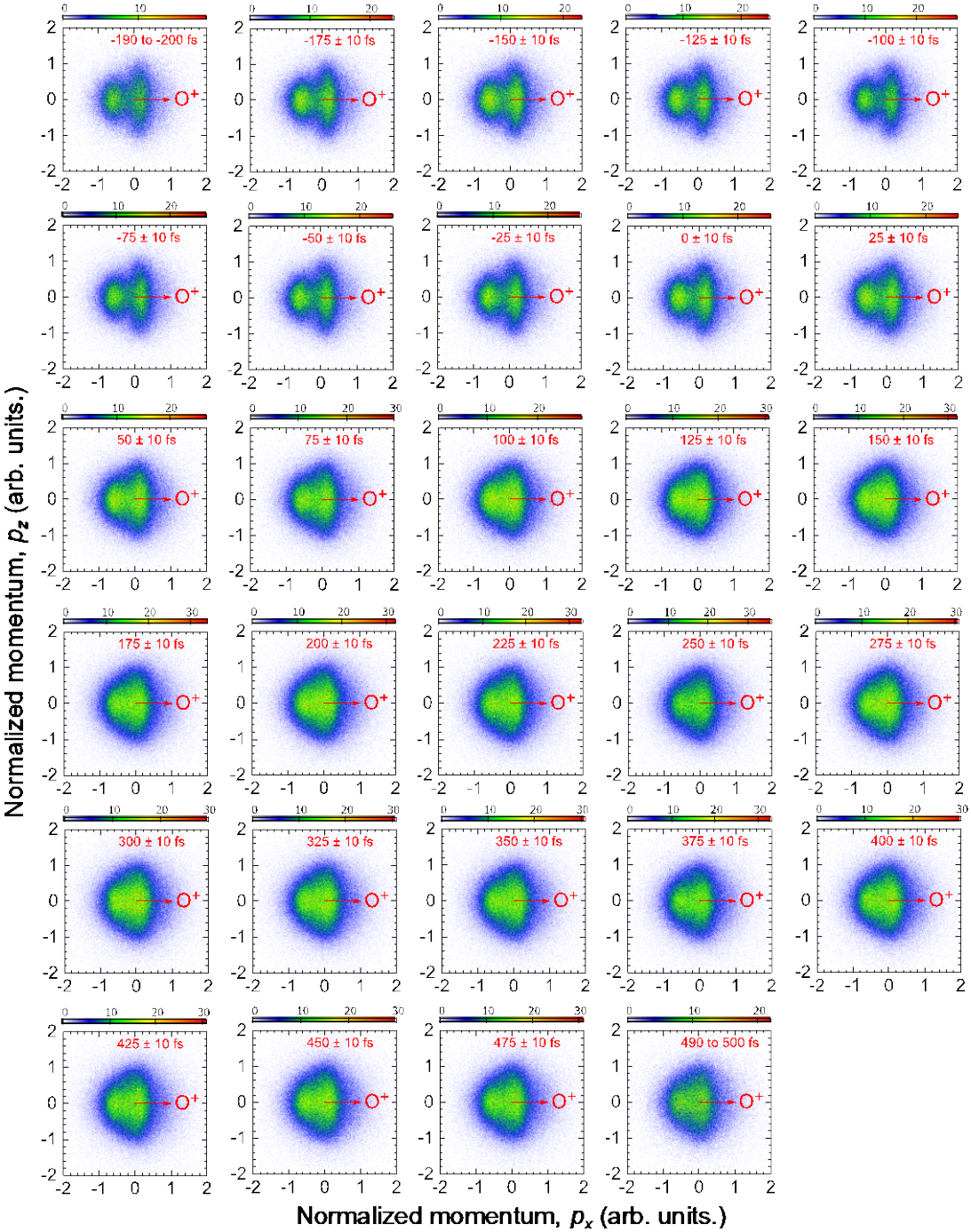

Figure S16: Experimental *normalized* Newton plots in the *px/pz* plane.

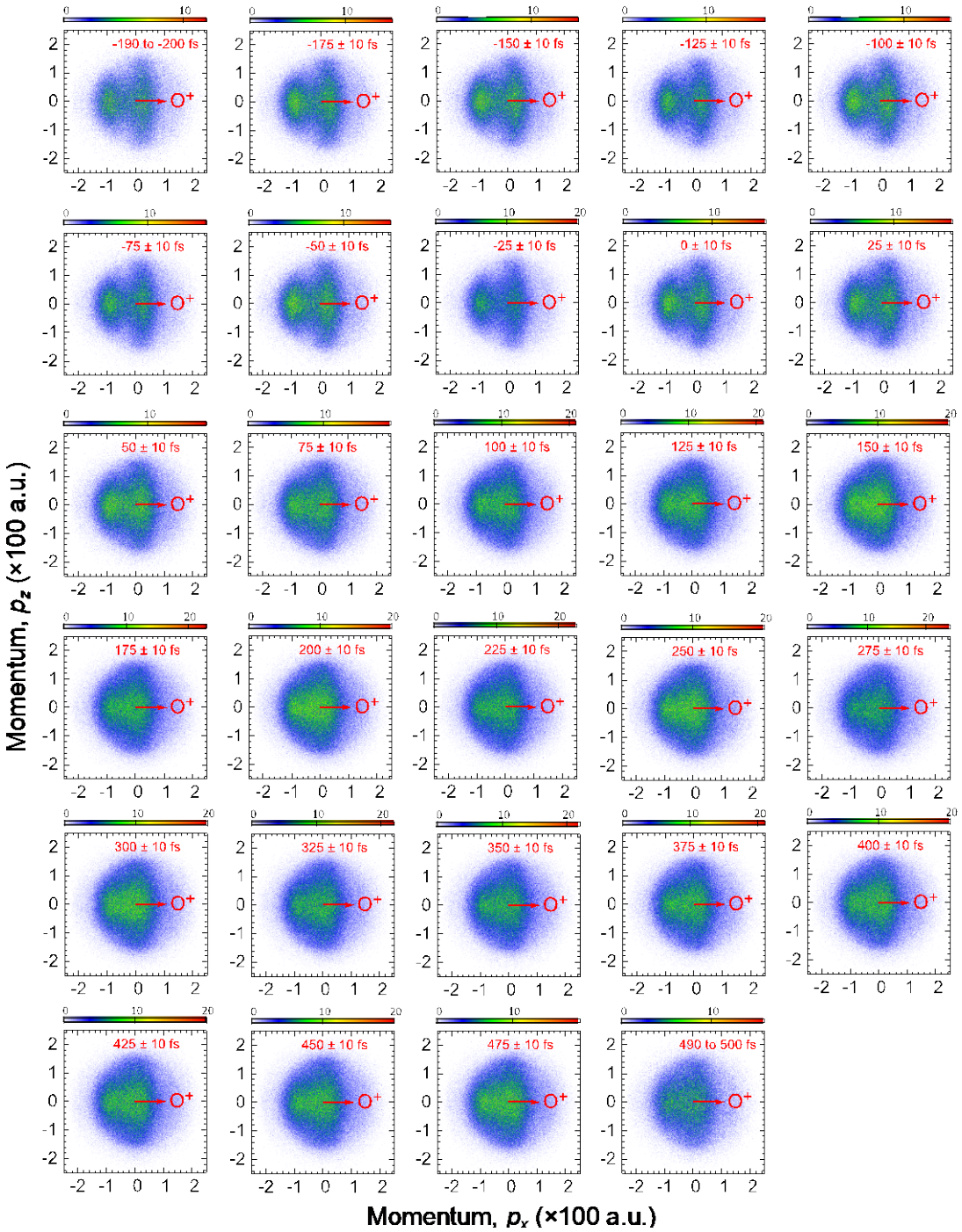

Figure S17: Experimental *non-normalized* Newton plots in the *px/pz* plane. Similar to **Figure S15**, the red arrow shows the emission direction of the O^+ reference ion, and the length of the arrow in this non-normalized plot was arbitrarily chosen for illustration purposes only.

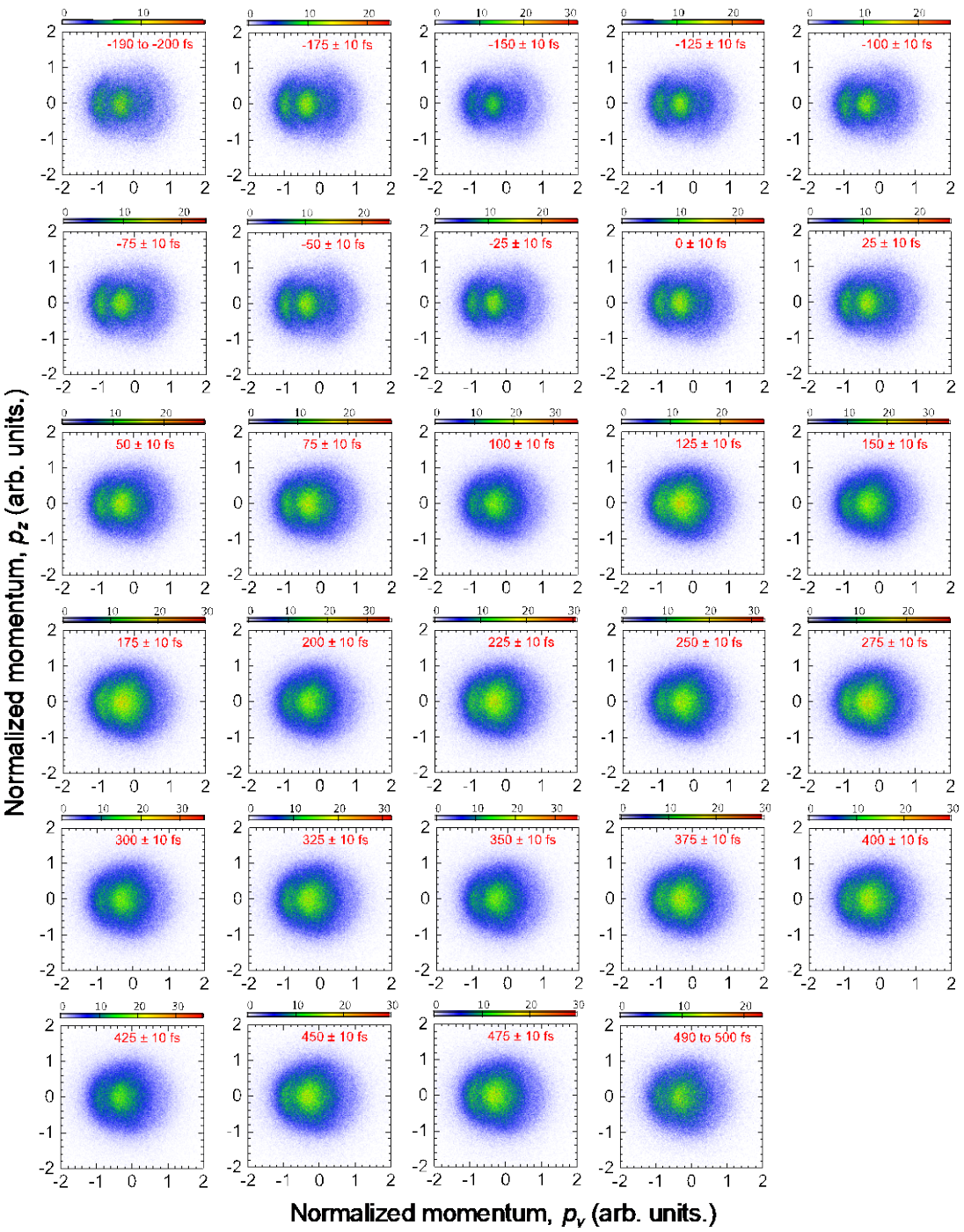

Figure S18: Experimental *normalized* Newton plots in the py/pz plane. The direction of the oxygen ion is perpendicular to the plane and crosses at the origin.

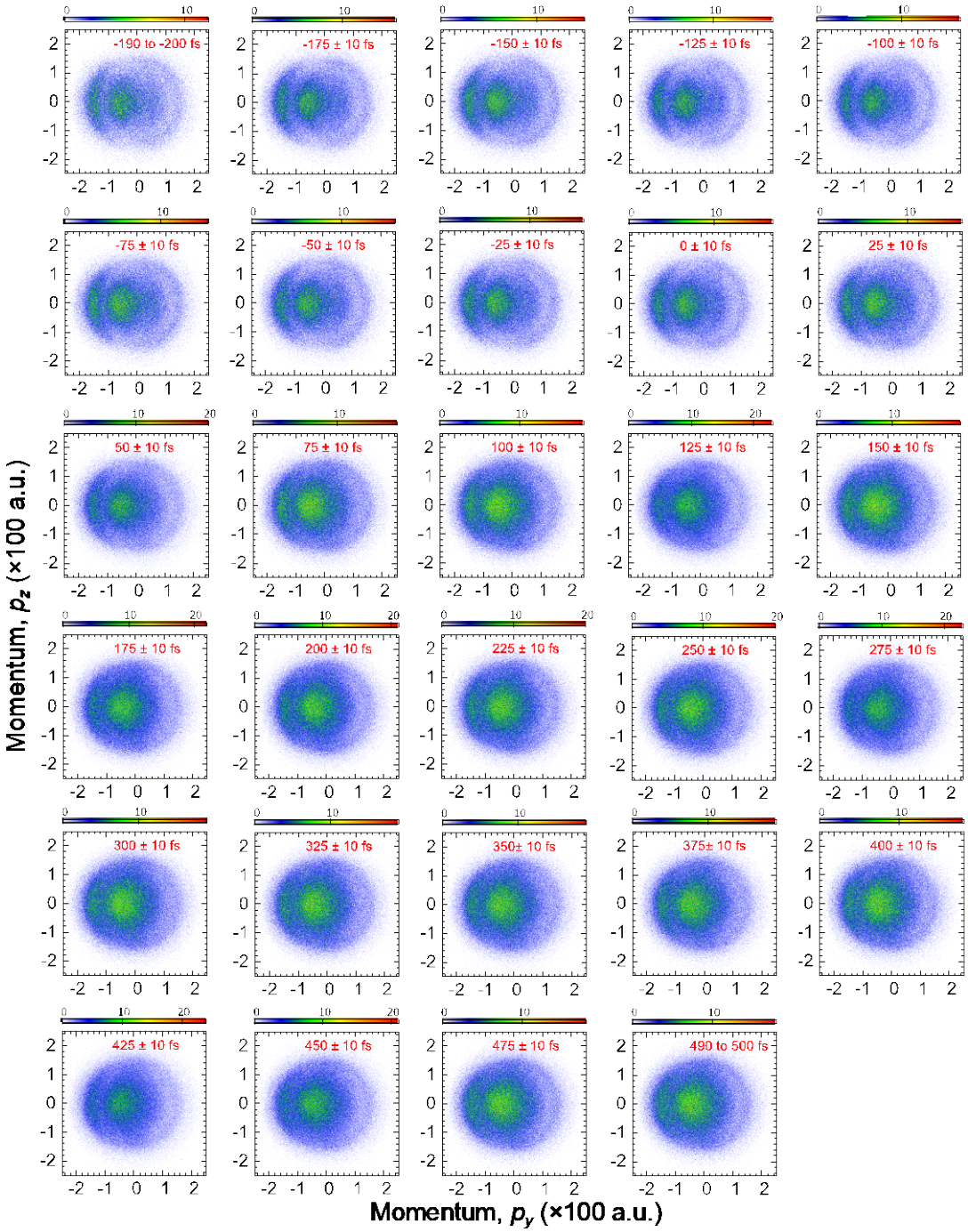

Figure S19: Experimental *non-normalized* Newton plots in the *py/pz* plane. The direction of the oxygen ion is perpendicular to the plane and crosses at the origin.

11. Simulated normalized Newton plots for the $4C^+ + O^+$ channel in the *px/py* plane

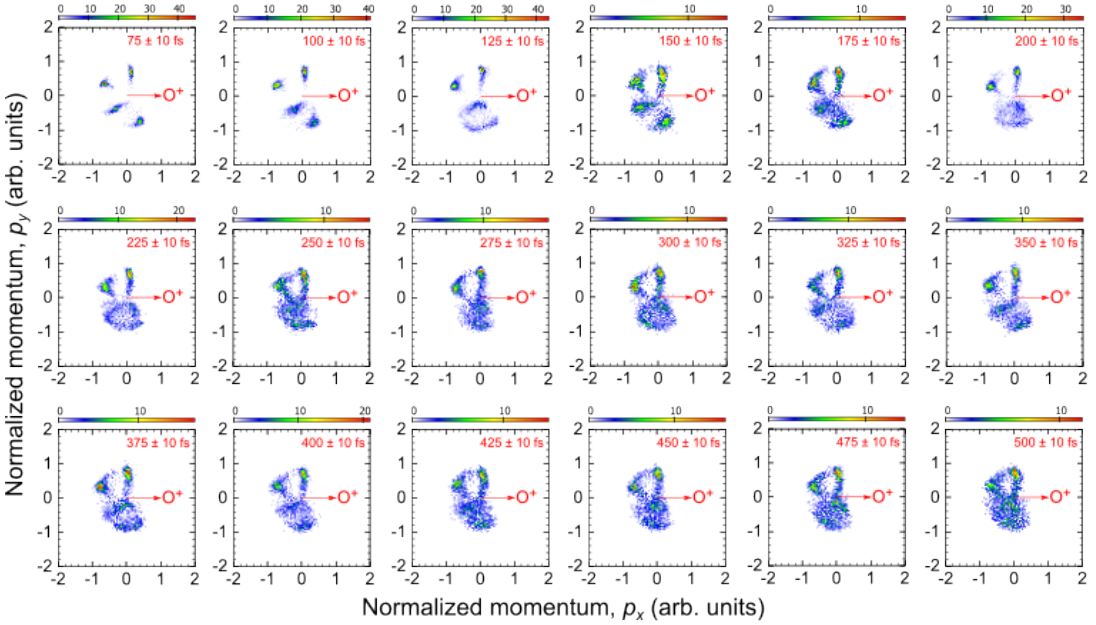

Figure S20: Simulated Newton plots from the ground-state trajectories binned in time step of 25 fs when assuming *no* initial internal energy at the start of the AIMD simulations.

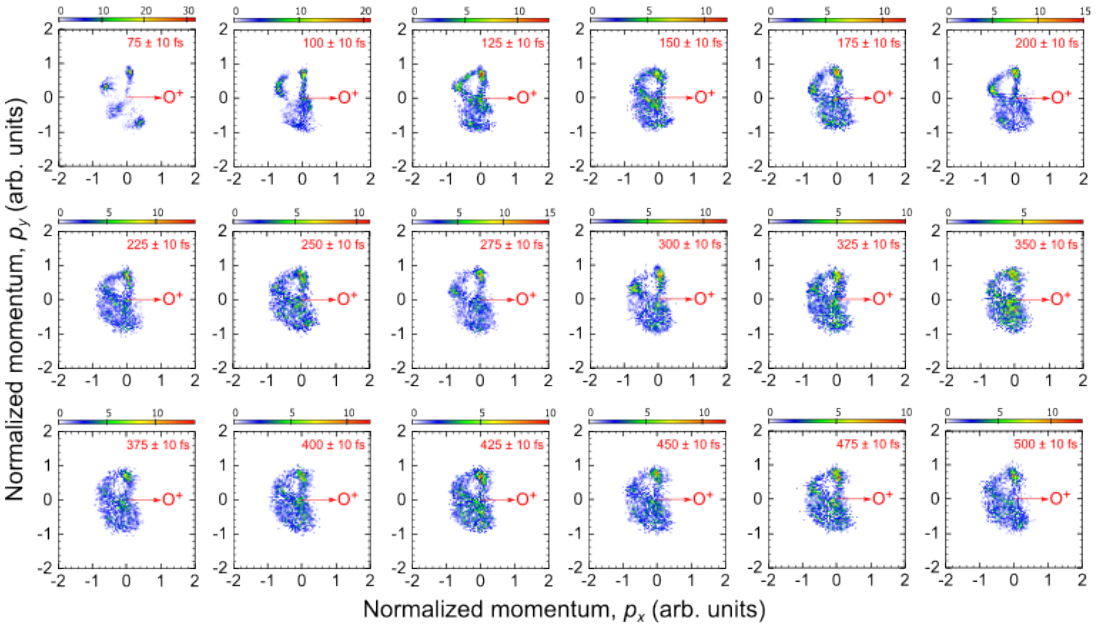

Figure S21: Simulated Newton plots from the ground-state trajectories binned in time step of 25 fs when assuming an initial internal energy of 2.5 eV at the start of the AIMD simulations.

12. Average momentum of the carbon ion with the lowest kinetic energy

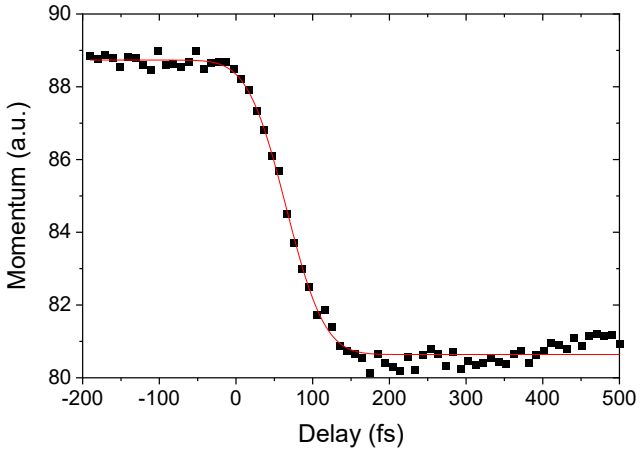

Equation	$A + B * \mathrm{erf}(\frac{x - xc}{w})$
A	84.7 ± 0.03
B	-4.04 ± 0.04
xc	65.4 ± 1.27
w	55.8 ± 2.45

Figure S22: Average momentum as a function of delay of the carbon ion with the lowest kinetic energy along with an *erf* fit to the experimental data and the resulting fit parameters.

13. Supplementary movies

Supplementary movie 1.avi: 3-dimensional animation of the ring-opening trajectory on the excited electronic state, as displayed in Fig. S7(d).

Supplementary movie 2.avi: 3-dimensional animation of the trajectory from the ring-opening conical intersection to the ring-opened isomer on the ground electronic state.

References

1 M. J. Frisch, G. W. T., H. B. Schlegel, G. E. Scuseria, M. A. Robb, J. R. Cheeseman, G. Scalmani, V. Barone, G. A. Petersson, H. Nakatsuji, X. Li, M. Caricato, A. Marenich, J. Bloino, B. G. Janesko, R. Gomperts, B. Mennucci, H. P. Hratchian, J. V. Ortiz, A. F. Izmaylov, J. L. Sonnenberg, D. Williams-Young, F. Ding, F. Lipparini, F. Egidi, J. Goings, B. Peng, A. Petrone, T. Henderson, D. Ranasinghe, V. G. Zakrzewski, J. Gao, N. Rega, G. Zheng, W. Liang, M. Hada, M. Ehara, K. Toyota, R. Fukuda, J. Hasegawa, M. Ishida, T. Nakajima, Y. Honda, O. Kitao, H. Nakai, T. Vreven, K. Throssell, J. A. Montgomery, Jr., J. E. Peralta, F. Ogliaro, M. Bearpark, J. J. Heyd, E. Brothers, K. N. Kudin, V. N. Staroverov, T. Keith, R. Kobayashi, J. Normand, K. Raghavachari, A. Rendell, J. C. Burant, S. S. Iyengar, J. Tomasi, M. Cossi, J. M. Millam, M. Klene, C. Adamo, R. Cammi, J. W. Ochterski, R. L. Martin, K. Morokuma, O. Farkas, J. B. Foresman, and D. J. Fox. *Gaussian 09 Rev B.01*. (Gaussian, Inc., 2009.).

2 Oesterling, S. *et al.* Substituent effects on the relaxation dynamics of furan, furfural and β-furfural: a combined theoretical and experimental approach. *Phys. Chem. Chem. Phys.* **19**, 2025-2035 (2017).

3 Turney, J. M. *et al.* Psi4: an open-source ab initio electronic structure program. *WIREs Computational Molecular Science* **2**, 556-565 (2012).

4 Barbatti, M. *et al.* Newton-X: a surface-hopping program for nonadiabatic molecular dynamics. *WIREs Comput. Mol. Sci.* **4**, 26-33 (2014).

5 Schlegel, H. B. *et al.* Ab initio molecular dynamics: Propagating the density matrix with Gaussian orbitals. *J. Chem. Phys.* **114**, 9758-9763 (2001).

6 Iyengar, S. S. *et al.* Ab initio molecular dynamics: Propagating the density matrix with Gaussian orbitals. II. Generalizations based on mass-weighting, idempotency, energy conservation and choice of initial conditions. *J. Chem. Phys.* **115**, 10291-10302 (2001).

7 Schlegel, H. B. *et al.* Ab initio molecular dynamics: Propagating the density matrix with Gaussian orbitals. III. Comparison with Born–Oppenheimer dynamics. *J. Chem. Phys.* **117**, 8694-8704 (2002).

8 Fuji, T. *et al.* Ultrafast photodynamics of furan. *J. Chem. Phys.* **133**, 234303 (2010).